




# MoO<sub>3</sub> nanoplates: a high-capacity and long-life anode material for sodium-ion batteries

Caihong Yang<sup>1,4</sup>, Qiankun Xiang<sup>1,4</sup>, Xuemei Li<sup>1,4</sup>, Yanqi Xu<sup>1</sup>, Xin Wang<sup>3</sup>, Xiangli Xie<sup>2</sup>, Cunjun Li<sup>1</sup>, Hai Wang<sup>1,\*</sup>, and Linjiang Wang<sup>1,5,\*</sup> 

<sup>1</sup> College of Materials Science and Engineering, Guilin University of Technology, Guilin 541004, China

<sup>2</sup> College of Chemistry and Bioengineering, Guilin University of Technology, Guilin 541004, China

<sup>3</sup> Key Laboratory of Materials Physics, Institute of Solid State Physics, Chinese Academy of Sciences, Hefei 230031, China

<sup>4</sup> Key Laboratory of New Processing Technology for Nonferrous Metal & Materials, Ministry of Education, Guilin University of Technology, Guilin 541004, China

<sup>5</sup> Collaborative Innovation Center for Exploration of Hidden Nonferrous Metal Deposits and Development of New Materials in Guangxi, Guilin University of Technology, Guilin 541004, China

Received: 5 March 2020

Accepted: 4 May 2020

Published online:

14 May 2020

© Springer Science+Business Media, LLC, part of Springer Nature 2020

## ABSTRACT

MoO<sub>3</sub> has become a very promising energy storage material owing to its high theoretical capacity and layered structure. However, MoO<sub>3</sub> suffers from low specific capacitance and fast degradation performance due to pulverization caused by volume change during discharge and charge process. Here, we report the MoO<sub>3</sub> nanoplates (MoO<sub>3</sub> NPs) from Mo-based metal–organic frameworks (Mo-MOFs) via a facile heating treatment. When used as an anode in sodium-ion batteries (SIBs), the material showed 154 mAh g<sup>-1</sup> superior discharge capacity at 50 mA g<sup>-1</sup> after 1200 cycles. Even at 500 mA g<sup>-1</sup>, it also showed 217 mAh g<sup>-1</sup> high specific capacity after 500 cycles. This specific MoO<sub>3</sub> material design strategy offers suitable conditions for relieving the volume expansion and provides multiple channels for Na<sup>+</sup> transport and electron transfer in MoO<sub>3</sub> during discharge and charge process. This work highlights the importance of MoO<sub>3</sub> nanoplates in preventing the pulverization caused by volume expansion in SIBs.

## Introduction

Lithium-ion batteries are widespread, but their price will likely increase due to limited lithium resources [1]. Thus, it is necessary to find new elements that can substitute for lithium to reduce costs. Sodium is

abundant with similar electrochemical properties as lithium [2]. However, the choice of electrode materials for sodium-ion batteries (SIBs) is limited because of the larger ionic radius of sodium. This leads to slow Na<sup>+</sup> kinetic reactions and significant pulverization [3]. Therefore, finding suitable materials with a stable structure remains a challenge for SIBs.

Address correspondence to E-mail: hbwanghai@gmail.com; wlinjiang@163.com

Transition metal oxides such as  $\text{Fe}_3\text{O}_4$  [4],  $\text{Co}_3\text{O}_4$  [5],  $\text{NiO}$  [6],  $\text{ZnO}$  [7] and  $\text{MoO}_3$  [8] have been widely studied as electrode materials for SIBs because of their suitable reaction potential with sodium ion and high theoretical capacity. Of these,  $\text{MoO}_3$  is an environmentally friendly and low-cost anode material delivering a high capacity ( $1117 \text{ mAh g}^{-1}$ ) by insertion and conversion reactions [9]. More importantly, the layered structure of  $\text{MoO}_3$  offers insertion locations and  $\text{Na}^+$  diffusion channels [10, 11]. However, like most other high-capacity anode materials,  $\text{MoO}_3$  suffers from a low specific capacitance and fast degradation performance due to the pulverization caused by significant dimensional and volume changes during repeat cycling [12, 13]. To overcome these problems,  $\text{MoO}_3$  can be composited with a protective layer (carbon [14], graphene [15] or glucose [16]). Researchers have also designed different nanomorphologies (nanobelt [17, 18], nanoparticle [19], nanotube [20], nanowire [21] and nanoplate [13, 22]). In our previous work [16], nanocomposites composed of  $\text{MoO}_{3-x}$  and glucose were used as a lithium anode. These materials facilitate a pulverized particle reaction in a confined space to ensure electrical contact between the pulverized particles. Unfortunately, this method does not fundamentally solve the pulverization problem. However, the nanomorphology design may fundamentally alleviate the pulverization problem caused by stress. Currently, the design of nanoplate structures has attracted much attention in stress relief due to their great structural flexibility and surface properties [13, 22, 24]. Wu et al. [13] prepared  $\text{MoO}_3$  nanoplate arrays via  $\text{MoS}_2$  as a template. This material showed  $2.1 \text{ mAh cm}^{-2}$  high specific capacity at  $0.2 \text{ mA cm}^{-2}$  after 200 cycles in SIBs. Cao et al. [22] reported  $\text{MoO}_3$  nanoplates within foam-like carbon nanoflakes via calcining precursor as an anode for lithium-ion batteries. This material delivered  $791 \text{ mAh g}^{-1}$  after 100 cycles at  $500 \text{ mA g}^{-1}$ . The  $\text{MoO}_3$  NPs were synthesized with a relatively uniform size by  $\text{MoS}_2$  templates. However, the use of  $\text{MoS}_2$  templates generates noxious gases such as  $\text{H}_2\text{S}$  and  $\text{NH}_3$ . This is not conducive to large-scale commercial production and is environmentally dangerous. Therefore, the environmentally friendly templates are still needed.

Recently, metal–organic frameworks (MOFs) have received intense interest as self-templates for the synthesis of material with different morphologies [24]. Here, we report  $\text{MoO}_3$  nanoplates ( $\text{MoO}_3$  NPs)

from Mo-based metal–organic frameworks (Mo-MOFs) by facile calcination treatment. The  $\text{MoO}_3$  NPs can relieve the volume expansion and maintain structural stability during repeated cycling. To better illustrate the advantages of the nanoplate structure in preventing pulverization,  $\text{MoO}_3$  nanobelts ( $\text{MoO}_3$  NBs) were synthesized by hydrothermal method for comparison. When two electrodes were used as an anode for SIBs, the  $\text{MoO}_3$  NPs offered a higher discharge capacity of  $154 \text{ mAh g}^{-1}$  at  $50 \text{ mA g}^{-1}$  after 1200 cycles than  $\text{MoO}_3$  NBs ( $49 \text{ mAh g}^{-1}$ ). To further investigate the structural stability of  $\text{MoO}_3$  NPs, the micromorphology of both electrodes was evaluated after discharge–charge. This work offers new insight into the design of structural morphologies that prevent pulverization in anode materials during repeated cycling.

## Materials and methods

### Preparation of molybdenum-based metal–organic frameworks (Mo-MOFs)

Mo-MOFs were prepared based on the previous literature [25]. 3.5 g commercial  $\text{MoO}_3$  and 1.66 g imidazole were dispersed into 250 mL deionized (DI) water with string for 10 min. The compound was refluxed under sequential string at  $75^\circ\text{C}$  for 12 h. After the reaction finished, the white precipitates of Mo-MOFs were washed and centrifuged several times with DI water. The white powders were obtained after drying overnight in air at  $60^\circ\text{C}$ .

### Preparation of $\text{MoO}_3$ nanoplates

The  $\text{MoO}_3$  nanoplates ( $\text{MoO}_3$  NPs) were obtained from the Mo-MOFs by calcination at  $450^\circ\text{C}$  for 2 h (air atmosphere) with the heating rate of  $5^\circ\text{C min}^{-1}$ . In order to study the change process of  $\text{MoO}_3$  NPs with the temperature increase, the Mo-MOFs were heated at  $300^\circ\text{C}$  and  $600^\circ\text{C}$ ; followed by the aforementioned process, the products were denoted as Mo-MOFs-C300 and Mo-MOFs-C600.

### Preparation of $\text{MoO}_3$ nanobelts

Preparation of  $\text{MoO}_3$  nanobelts: The  $\text{MoO}_3$  nanobelts ( $\text{MoO}_3$  NBs) were prepared by a hydrothermal treatment method following our previous report [16].

In a typical procedure, 2 g ammonium molybdate ( $(\text{NH}_4)_6\text{Mo}_7\text{O}_{24}\cdot 4\text{H}_2\text{O}$ ) was dissolved into 60 mL DI water to form homogeneous solution with continuous stirring. Then, adding 12 mL  $\text{HNO}_3$  to the above solution by dropper. After stirring for 1 h, the homogeneous solution was transferred into a 100-mL Teflon-lined autoclave, and the autoclave was placed in an oven at 180 °C for 24 h. After the reaction finished, the products were washed and centrifuged by DI water for several times. The as-synthesized white products were obtained after drying at 60 °C for 12 h in an oven.

### Characterizations

The microstructures of samples were tested by field emission scanning electron microscope (FESEM, JEOL JSM 6300, Tokyo, Japan) and transmission electron microscopy (TEM, JEOL, JEM-2010F, 200 kV, Japan). X-ray diffractometer (XRD) measurement of all samples was taken using a PANalytic X'Pert spectrometer with wavelength of 0.15405 nm. X-ray photoelectron spectroscopy was carried out to confirm the chemical state and bonding situations of all electrode materials (XPS, VG ESCALAB 210 electron spectrometer). The Brunauer–Emmett–Teller (BET, Micromeritics ASAP 2020) was used to obtain nitrogen adsorption–desorption isotherms and pore size distribution of all samples. The Fourier transform infrared spectroscopy (FTIR, Thermo Fisher Scientific Inc., USA) measurement was taken using KBr as the dispersant. The micro-Raman spectroscopy measurement was taken with an excitation wavelength of 532 nm (USA, Thermo Fisher Scientific DXR). The Keithley 4200 SCS and a micro-manipulator 6150 probe station were used to obtain the I–V curves of all samples.

### Electrochemical measurements

The working electrode was made by mixing as-prepared samples, conductive additive (acetylene black) as well as binder (PVDF) at a weight ratio of 7:2:1 in N-methyl pyrrolidone (NMP) solvent to form good fluidity slurry with continuous stirring.

After that, the slurry was coated on the copper foil. Then, the copper foil with slurry was placed in vacuum oven at 90 °C for overnight. After drying, the electrode films were cut into a 14-mm-diameter disk with 1–2 mg electrode material on it. The coin cells

(CR2032) were assembled in glove box filled with argon. The separator is Celgard 3400 microporous membrane. The electrolyte is 1.0 M  $\text{NaClO}_4$  with 1:1 ratio ethylene carbonate (EC) and diethyl carbonate as additive (by volume, Novolyte Technologies, USA). The electrochemical performance of assembled batteries was tested in an incubator (25 °C). The performance of cyclic voltammetry (CV) and electrochemical impedance spectroscopy (EIS) was tested by electrochemical workstation (CHI 760E, Shanghai, China). The cycling stability and rate capability was obtained by battery testing system (NEWARE).

### Results and discussion

Figure 1a shows the synthesis of  $\text{MoO}_3$  NPs—their growth changes with increasing temperature. The  $\text{MoO}_3$  NPs were first synthesized from Mo-MOFs in a facile and green way. The micro-rodlike morphology (Fig. S1a) and XRD pattern (Fig. 1b) of Mo-MOFs are both consistent with the previous literature and confirm the successful preparation of Mo-MOFs [25]. After 300 °C treatment for 2 h (Mo-MOFs-C300), the morphology of Mo-MOFs is destroyed with many ordered nanorods appearing on the damaged surface; the structure of  $\text{MoO}_3$  is gradually formed with growth of (020), (040) and (060) peaks in the XRD pattern. The nanoplate morphology (Fig. 2) of  $\text{MoO}_3$  is complete when the temperature increased to 450 °C, and the XRD pattern of the  $\text{MoO}_3$  NPs (Fig. 1b) nicely agrees with the JCPDS (05-0508). The intensity of (020), (040) and (060) peaks in the XRD pattern of  $\text{MoO}_3$  NPs is lower than that of  $\text{MoO}_3$  NBs (hydrothermal method), indicating that the  $\text{MoO}_3$  NBs have stronger anisotropic characteristics than  $\text{MoO}_3$  NPs—this may be critical to preparing nanoplates [26, 27]. It is noted that the intensity of (020), (040) and (060) peaks in the XRD pattern of commercial  $\text{MoO}_3$  is also lower than that of  $\text{MoO}_3$  NBs. This reveals that the  $\text{MoO}_3$  NBs also have stronger anisotropic characteristics than commercial  $\text{MoO}_3$ . This result may explain that the commercial  $\text{MoO}_3$  is not a belt morphology (Fig. S3). At 600 °C, the XRD patterns (Fig. 1b) show that the product is still  $\text{MoO}_3$  (named as Mo-MOFs-C600), but the micromorphology (Fig. S1c) is not as uniform as with  $\text{MoO}_3$  NPs (at 450 °C for 2 h). These results suggest that 450 °C is a suitable temperature to synthesize uniform  $\text{MoO}_3$

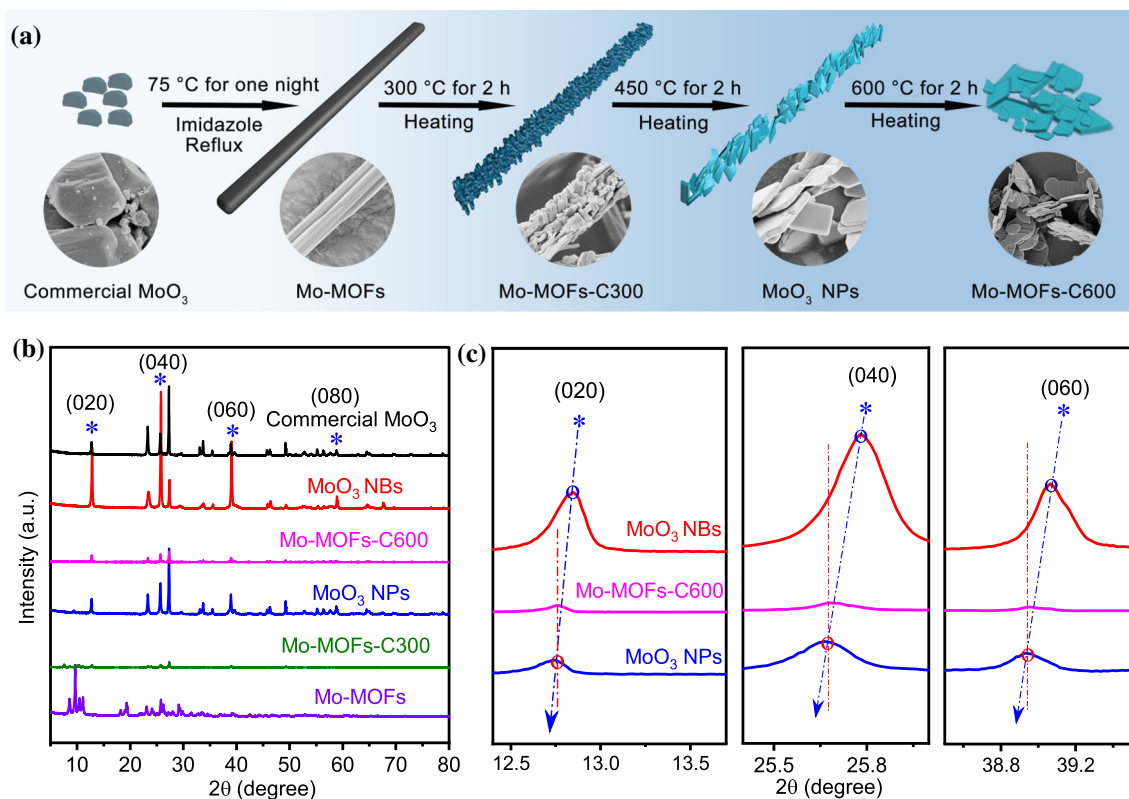
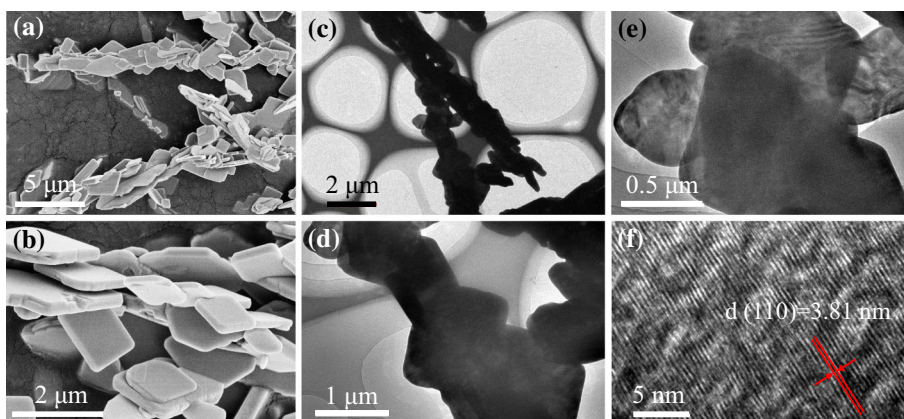


**Figure 1** a Diagram of MoO<sub>3</sub> NPs synthesis process with the temperature increase and the corresponding FESEM images (inset); b XRD patterns of Mo-MOFs, Mo-MOFs-C300, MoO<sub>3</sub> NPs,

Mo-MOFs-C600, MoO<sub>3</sub> NBs and commercial MoO<sub>3</sub>; c selected XRD pattern insets of the (020), (040) and (060) diffraction peaks that compare MoO<sub>3</sub> NPs, Mo-MOFs-C600 and MoO<sub>3</sub> NBs, respectively.

**Figure 2** FESEM image (a, b) and TEM images (c, d, e, f) of MoO<sub>3</sub> NPs.



NPs. Moreover, the (020), (040) and (060) peaks of the Mo-MOFs-C600 are little discernable shift compared with the MoO<sub>3</sub> NPs (450 °C) (Fig. 1c). This suggest that there is no causal relationship between layer spacing and temperature. However, further analyzing the data in Fig. 1c, the (020), (040) and (060) peaks of the MoO<sub>3</sub> NPs are shifted toward lower angles in comparison with MoO<sub>3</sub> NBs, which indicate that MoO<sub>3</sub> NPs have a larger interlayer spacing than

MoO<sub>3</sub> NBs. The increscent interlayer spacing offers more diffusion channels for sodium ions and electrons [28].

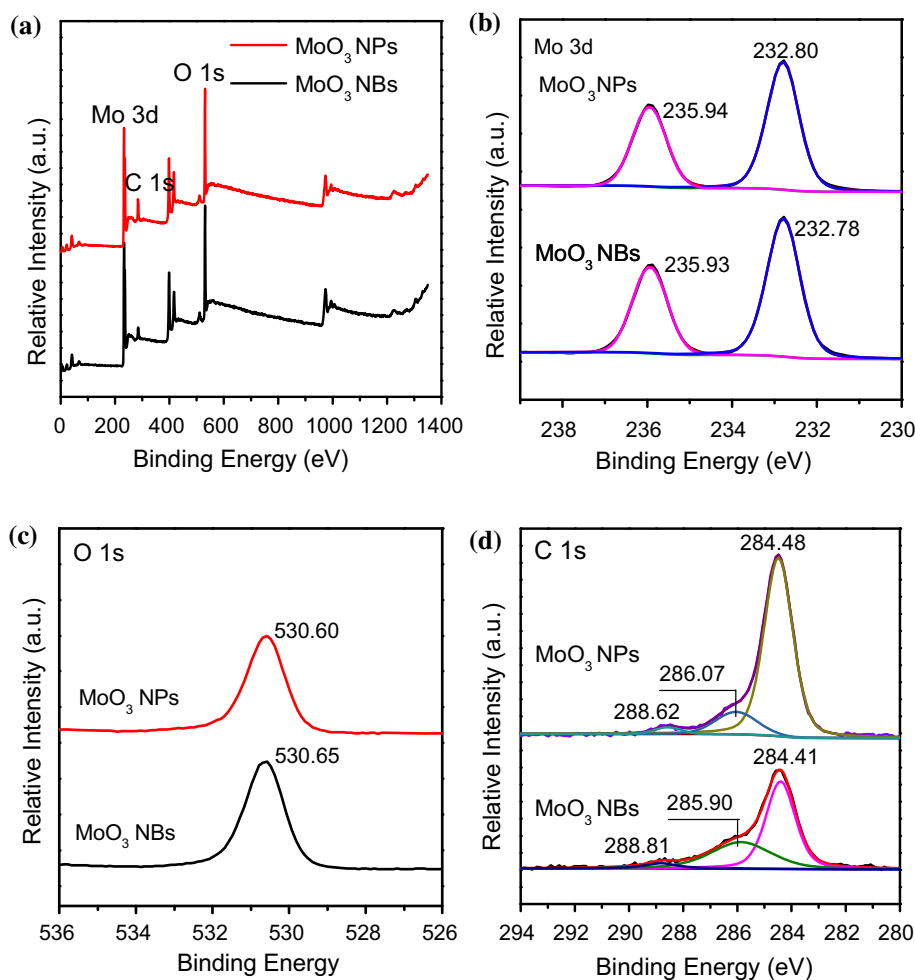
XPS was performed to further study the chemical states of MoO<sub>3</sub> NPs (Fig. 3a–d). The XPS survey spectrum reveals the existence of Mo, O and C (Fig. 3a). The high-resolution Mo 3d spectrum (Fig. 3b) revealed two peaks located at 232.80 and 235.94 eV, which is accord well with Mo3d<sup>5/2</sup> and

Mo3d<sup>3/2</sup> of the oxidation state (Mo<sup>6+</sup>) of MoO<sub>3</sub> NPs, respectively. In the O 1s XPS spectrum (Fig. 3c), the Mo–O bond of MoO<sub>3</sub> NPs is deconvoluted with binding energies at 530.60 eV [29]. It is well known that carbon can directly enhance the electrical conductivity of the electrode [30]. Moreover, the MoO<sub>3</sub> NPs are prepared from Mo-MOFs. Therefore, it is necessary to identify the C 1s spectrum to confirm whether carbon exists in the MoO<sub>3</sub> NPs. Figure 3d shows three typical peaks: C–C (284.48, 284.41 eV), C–O (286.07, 285.9 eV) and C=O (288.62, 288.81 eV) [31]. Comparing the peak position of the C 1s XPS spectrum between MoO<sub>3</sub> NBs and MoO<sub>3</sub> NPs, the difference in the position of the corresponding peak is lower 0.2 V, and the atomic percentage of C 1s in MoO<sub>3</sub> NBs and MoO<sub>3</sub> NPs is approximate (20.76% vs. 29.12%) (Table S1). Therefore, it is possible that the C 1s of XPS is adventitious carbon. To verify this hypothesis, FTIR and Raman spectra were also analyzed (Fig. S4). The FTIR analysis shows that the

spectra of MoO<sub>3</sub> NPs and MoO<sub>3</sub> NBs are nearly identical (Fig. S4a). However, what is surprising is that the Raman spectrum (Fig. S4b) has an inconspicuous G-band and D-band of the carbon substrate. One possible reason for this is that a small amount of carbon/MoO<sub>3</sub> NPs composition may exist in MoO<sub>3</sub> NPs. TGA is further analyzed to confirm the carbon content in the MoO<sub>3</sub> NPs (Fig. S4c). The results suggest that the content of carbon and H<sub>2</sub>O is 0.153%. Hence, the carbon content can be ignored in the MoO<sub>3</sub> NPs. This reasonably assumes that carbon will not affect the electrochemical performance of MoO<sub>3</sub> NPs.

The electrochemical performance of MoO<sub>3</sub> NPs has been evaluated as an anode for SIBs. Figure 4a shows the cyclic voltammetry (CV) of the MoO<sub>3</sub> NPs within 0.1–3 V. The several reduction peaks observed in the first discharge vanish in the subsequent scans, suggesting an irreversible conversion reaction at the MoO<sub>3</sub> NPs electrode. There is one clear peak near

**Figure 3** XPS spectra of MoO<sub>3</sub> NBs and MoO<sub>3</sub> NPs: **a** survey spectrum, **b** Mo 3d, **c** O 1s and **d** C 1s for MoO<sub>3</sub> NBs and MoO<sub>3</sub> NPs.



2.4 V due to the formation of a solid electrolyte interphase (SEI) and insertion of  $\text{MoO}_3$  by  $\text{Na}^+$  to form  $\text{Na}_x\text{MoO}_3$  ( $\text{MoO}_3 + x\text{Na}^+ + xe^- \rightarrow \text{Na}_x\text{MoO}_3$ ). The peaks near 1.56 V and 1.01 V correspond to excess sodiation, leading to  $\text{Na}_{x+y}\text{MoO}_3$ . The potential below 0.5 V is due to the formation of Mo and  $\text{Na}_2\text{O}$  ( $\text{Na}_{x+y}\text{MoO}_3 + (6-x)\text{Na}^+ + (6-x)e^- \rightarrow \text{Mo} + 3\text{Na}_2\text{O}$ ) [8, 11, 32]. An anode peak located at 0.668 V is observed in first three charging cycles, indicating a reversible removal of the sodium ion [33]. Compared with  $\text{MoO}_3$  NBs (Fig. S5a), the integral area of  $\text{MoO}_3$  NPs is larger than that of  $\text{MoO}_3$  NBs, suggesting that  $\text{MoO}_3$  NPs have better electrochemical performance than  $\text{MoO}_3$  NBs. Figure 4b shows the discharge–charge curves of the  $\text{MoO}_3$  NPs. There are several distinct plateaus in the first discharging process. The plateaus disappear in subsequent cycles corresponding to the CV curves (Fig. 4a) [32]. Besides, the discharge capacity of  $\text{MoO}_3$  NBs are 727, 295, 125, 105, 83 and 49  $\text{mAh g}^{-1}$  at 1st, 2nd, 150th, 300th, 600th and 1200th, respectively (Fig. S5b); the discharge capacity of  $\text{MoO}_3$  NPs are up to 1222, 529, 247, 224, 185 and 154  $\text{mAh g}^{-1}$ , respectively (Fig. 4b). According to the calculations, the  $\text{MoO}_3$  NPs have a higher initial coulombic efficiency than

$\text{MoO}_3$  NBs (43.7% vs. 40.35%). Electrochemical impedance spectroscopy (EIS) was performed to compare the electrical conductivity and diffusion dynamics of  $\text{MoO}_3$  NBs and  $\text{MoO}_3$  NPs electrodes (Fig. 4c). Each Nyquist plot includes three parts: high-frequency semicircle, middle-frequency semicircle and low-frequency tail—these correspond to the sodium-ion migration impedance, charge transfer impedance and sodium-ion diffusion level, respectively [34]. The first and second semicircles of  $\text{MoO}_3$  NPs are much smaller than that of the  $\text{MoO}_3$  NBs, suggesting a lower ionic resistance and charge transfer resistance of  $\text{MoO}_3$  NPs. Moreover, the  $\text{MoO}_3$  NPs still have a lower resistance than  $\text{MoO}_3$  NBs after one cycle (Fig. S5c). Further I–V tests revealed that the conductivity of  $\text{MoO}_3$  NPs is preferable to  $\text{MoO}_3$  NBs (Fig. S6), which corresponds to the EIS results. This suggests that the introduction of the nanoplate structure and the expansion interlayer improves the conductivity of  $\text{MoO}_3$ . Figure 4e compares the cycling performance of  $\text{MoO}_3$  NBs and  $\text{MoO}_3$  NPs. The  $\text{MoO}_3$  NPs electrode delivers 154  $\text{mAh g}^{-1}$  high discharge capacity after 1200 cycles at a current density of 50  $\text{mA g}^{-1}$ , which is over threefold higher than  $\text{MoO}_3$  NBs (ca. 49  $\text{mAh g}^{-1}$ ). Even at the high

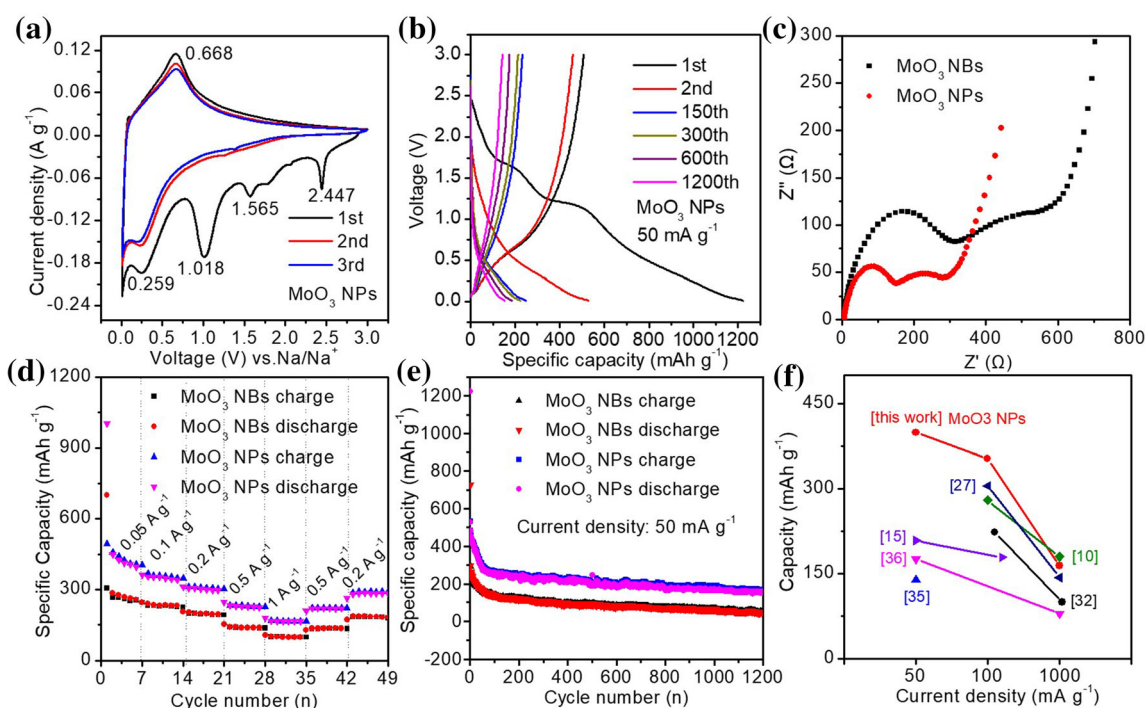


**Figure 4** Initial three CV curves of  $\text{MoO}_3$  NPs: **a** at 0.1  $\text{mV s}^{-1}$ ; **b** the discharge–charge curves at 50  $\text{mA g}^{-1}$ ; the Nyquist plots (**c**) and the rate capability (**d**) of  $\text{MoO}_3$  NBs and  $\text{MoO}_3$  NPs;

**e** cyclic performance of  $\text{MoO}_3$  NBs and  $\text{MoO}_3$  NPs at 50  $\text{mA g}^{-1}$ ; **f** electrochemical performance comparison of  $\text{MoO}_3$  NPs in this work with other  $\text{MoO}_3$ -based anodes previously reported for SIBs.

current density (500 mA g<sup>-1</sup>), the MoO<sub>3</sub> NPs retain 217 mAh g<sup>-1</sup> high discharge capacity after 500 cycles (Fig. S5d)). Particularly revealing is that the MoO<sub>3</sub> NPs also have excellent rate performance at different current densities (Fig. 4d). More importantly, the as-synthesized MoO<sub>3</sub> NPs have a high capacity and long cycle life compared with other MoO<sub>3</sub>-based anodes previously reported for SIBs (Fig. 4f, Table 1). In general, a high specific surface area is a key feature to improve electrochemical performance of electrode materials. Thus, Brunauer–Emmett–Teller (BET) analysis (Fig. S7) was performed to confirm whether MoO<sub>3</sub> NPs have a large specific surface area. Unfortunately, the MoO<sub>3</sub> NPs have a lower specific surface area (4.865 m<sup>2</sup> g<sup>-1</sup>) than MoO<sub>3</sub> NBs (7.168 m<sup>2</sup> g<sup>-1</sup>) (Table S2). Therefore, the structural stability of MoO<sub>3</sub> NPs is the key to perform excellent electrochemical performance.

To quantify the kinetics of both samples, scan rate-dependent cyclic voltammetry (Fig. 5a, b) was used to evaluate the capacitive contribution ( $k_1v$ ) and diffusion-controlled reactions ( $k_2v^{1/2}$ ) to the current response ( $I$ ) at a fixed potential ( $V$ ) according to the following formula [37]:

$$I(V) = k_1v + k_2v^{1/2},$$

where  $v$  is the scan rate. The pseudocapacitive effects of the MoO<sub>3</sub> NPs are higher than that of MoO<sub>3</sub> NBs at a scan rate of 0.1 mV s<sup>-1</sup> (21.9% vs. 16.8%) (Fig. 5c).

As the scan rate increases, the pseudocapacitive effects of MoO<sub>3</sub> NPs further increase up to 55.3% at 1 mV s<sup>-1</sup> (Fig. 5d). However, the MoO<sub>3</sub> NPs still show a low pseudocapacitive contribution. It is not surprising that the pseudocapacitive effects play a key role for small particles with a high specific surface area [38]. However, the size of MoO<sub>3</sub> NPs is a little large with a low surface area (4.8653 m<sup>2</sup> g<sup>-1</sup>) (Table S2). Besides, as shown in discharge–charge curves (Fig. 4b), the MoO<sub>3</sub> NPs electrode has several distinct plateaus corresponding to a lower section of pseudocapacitive effects [39].

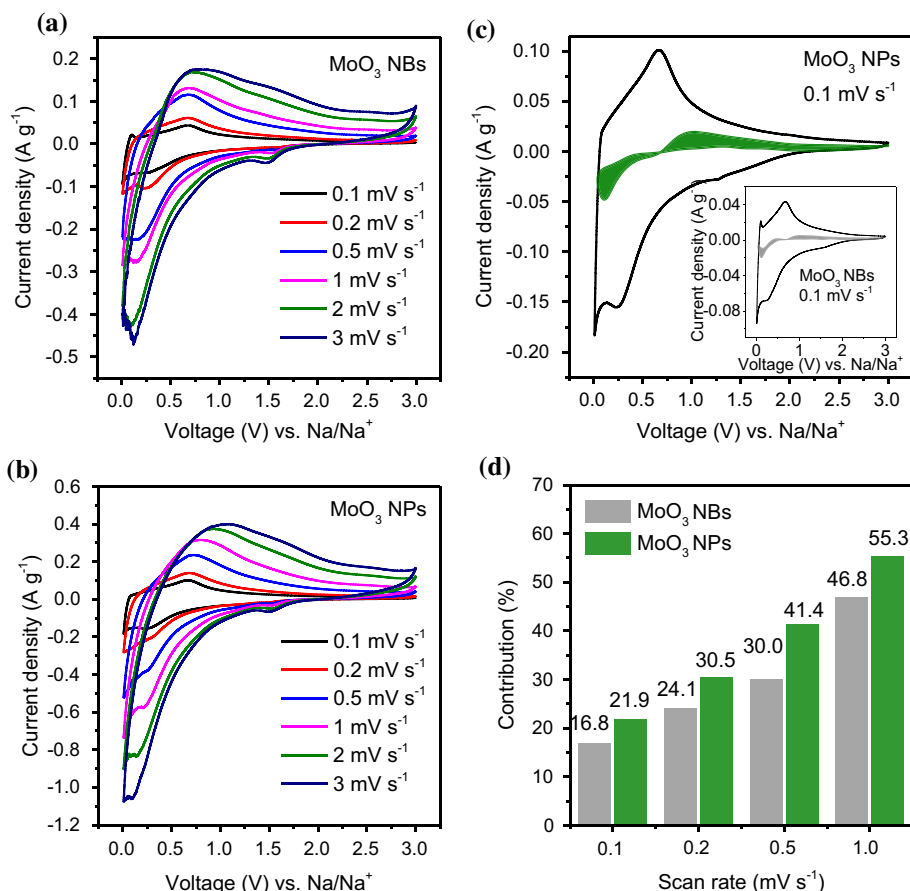
The excellent electrochemical performance of MoO<sub>3</sub> NPs can be explained by the stability of its electrode morphology during repeated cycles. To verify that the morphology of MoO<sub>3</sub> NPs is more stable than that of MoO<sub>3</sub> NBs during discharge–charge process, FESEM images of the two electrodes were compared after battery reactions. Figure 6a, b shows that the surface of both electrodes suffers from pulverization due to volume changes after 1 cycle. However, the microstructure of MoO<sub>3</sub> NPs (Fig. 6a) is clearly not as seriously damaged. After 10 cycles, the MoO<sub>3</sub> NPs electrode retains its nanoplate structure. Surprisingly, even after 1200 cycles, the complete nanoplate structure of MoO<sub>3</sub> NPs still can be observed. Except for the structural stability of the MoO<sub>3</sub> NPs itself, the MoO<sub>3</sub> NPs stability is also related to the high structural flexibility and surface

**Table 1** Electrochemical performance comparison of MoO<sub>3</sub> NPs in this work with other MoO<sub>3</sub>-based anodes previously reported for SIBs

Electrodes	Low rate capacity (mAh g <sup>-1</sup> )	High rate capacity (mAh g <sup>-1</sup> )	Cycling performance	Reference
a-MoO <sub>3</sub> NBs	280 (100 mA g <sup>-1</sup> )	188 (1000 mA g <sup>-1</sup> )	–	[10]
MoO <sub>3</sub> NSs	2.1 mAh cm <sup>-2</sup> (0.2 mA cm <sup>-2</sup> )	–	90% after 200 cycles (1 mA cm <sup>-2</sup> )	[13]
MoO <sub>3</sub> NSs / r-GO	208.2 (50 mA g <sup>-1</sup> )	178.7 (250 mA g <sup>-1</sup> )	–	[15]
a-MoO <sub>3</sub> MRs	305 (100 mA g <sup>-1</sup> )	143 (1000 mA g <sup>-1</sup> )	98% between 20–200 cycles (100 mA g <sup>-1</sup> )	[27]
a-MoO <sub>3</sub>	223.4 (213 mA g <sup>-1</sup> )	100 (1117 mA g <sup>-1</sup> )	55% over 500 cycles (558.5 mA g <sup>-1</sup> )	[32]
MoO <sub>3-x</sub> NSs	139 (50 mA g <sup>-1</sup> )	–	–	[35]
MoO <sub>3-x</sub>	176 (50 mA g <sup>-1</sup> )	79.2 (1000 mA g <sup>-1</sup> )	92% over 500 cycles (1000 mA g <sup>-1</sup> )	[36]
MoO <sub>3</sub> NPs	353 (100 mA g <sup>-1</sup> )	164 (1000 mA g <sup>-1</sup> )	63% between 100–1200 cycles (50 mA g <sup>-1</sup> )	This work
MoO <sub>3</sub> NBs	232 (100 mA g <sup>-1</sup> )	95 (1000 mA g <sup>-1</sup> )	35% between 100–1200 cycles (50 mA g <sup>-1</sup> )	This work

NBs nanobelts, NSs nanosheets, r-GO reduced graphene, MRs micro-rods, NPs nanoplates

**Figure 5** Cyclic voltammetry of MoO<sub>3</sub> NBs (a) and MoO<sub>3</sub> NPs (b) at different scan rates within 0.1 and 3 mV s<sup>-1</sup>; c capacitive contribution of MoO<sub>3</sub> NBs (inset) and MoO<sub>3</sub> NPs at scan rate of 0.1 mV s<sup>-1</sup>; d comparison of the capacitive contribution rate and diffusion controlled at various scan rates of MoO<sub>3</sub> NBs and MoO<sub>3</sub> NPs.



properties of the nanoplate structure. This can buffer the stress caused by volume changes during repeated cycles and then prevent pulverization, which eventually ensures the structural integrity of MoO<sub>3</sub> NPs. In contrast, the morphology of MoO<sub>3</sub> NBs (Fig. 6b) undergoes a huge change from the 1st to the 10th cycle, suffering tiny cracks at the 1st cycle, extensive cracking on the 2nd cycle and disintegration after 10 cycles. These results show that the MoO<sub>3</sub> NPs electrode maintains its integrity during repeated cycles leading to good contact between the electrode and the copper. This improves conductivity and provides multiple channels for Na<sup>+</sup> and electron transport [40–42]. These features are the keys by which MoO<sub>3</sub> NPs exhibit high reversible capacity and long-term stability.

The ex situ XRD (Fig. 7a, b) and XPS (Fig. 7d) spectra also provided insight into the electrochemical reversibility of the two electrodes. At the sodiation state (0.01 V) (Fig. 7a), the crystallinity of Na<sub>x</sub>MoO<sub>3</sub> (JCPDS 12-0773) in MoO<sub>3</sub> NPs is higher than that of MoO<sub>3</sub> NBs, which may be due to the high

transformation of MoO<sub>3</sub> NPs electrode during first sodiation process ( $\text{MoO}_3 + x \text{Na}^+ + x \text{e}^- \rightarrow \text{Na}_x \text{MoO}_3$ ) (Fig. 7c). Moreover, the higher peak of Na<sub>2</sub>O in MoO<sub>3</sub> NPs electrode than that of MoO<sub>3</sub> NBs electrode is observed. This suggests that more Na<sup>+</sup> move in the Na<sub>x</sub>MoO<sub>3</sub> to form Na<sub>2</sub>O (JCPDS 02-1288) and Mo (JCPDS 01-1207) ( $\text{Na}_x \text{MoO}_3 + (6-x) \text{Na}^+ + (6-x) \text{e}^- \rightarrow \text{Mo} + 3\text{Na}_2\text{O}$ ) (Fig. 7c) during the further sodiation processes. At the desodiation state (at 3 V) (Fig. 7b), both MoO<sub>3</sub> NBs and MoO<sub>3</sub> NPs electrodes appeared weak diffraction peaks of Mo and Na<sub>2</sub>O. Moreover, the diffraction peaks of Na<sub>2</sub>O in MoO<sub>3</sub> NPs are slightly lower than that of MoO<sub>3</sub> NBs. We come to the conclusion that higher transformation of MoO<sub>3</sub> NPs electrode compared with MoO<sub>3</sub> NBs, according to the conversion reaction equation:  $\text{Mo} + \text{Na}_2\text{O} \rightarrow \text{Na}_x \text{MoO}_3$ . It is found that the diffraction peaks of Na<sub>x</sub>MoO<sub>3</sub> in MoO<sub>3</sub> NBs are higher than that of MoO<sub>3</sub> NPs. This may be that the total of as-formed Na<sub>x</sub>MoO<sub>3</sub> is the sum of the Na<sub>x</sub>MoO<sub>3</sub> during the first sodiation and desodiation process. The crystallinity of MoO<sub>3</sub> phase in MoO<sub>3</sub>



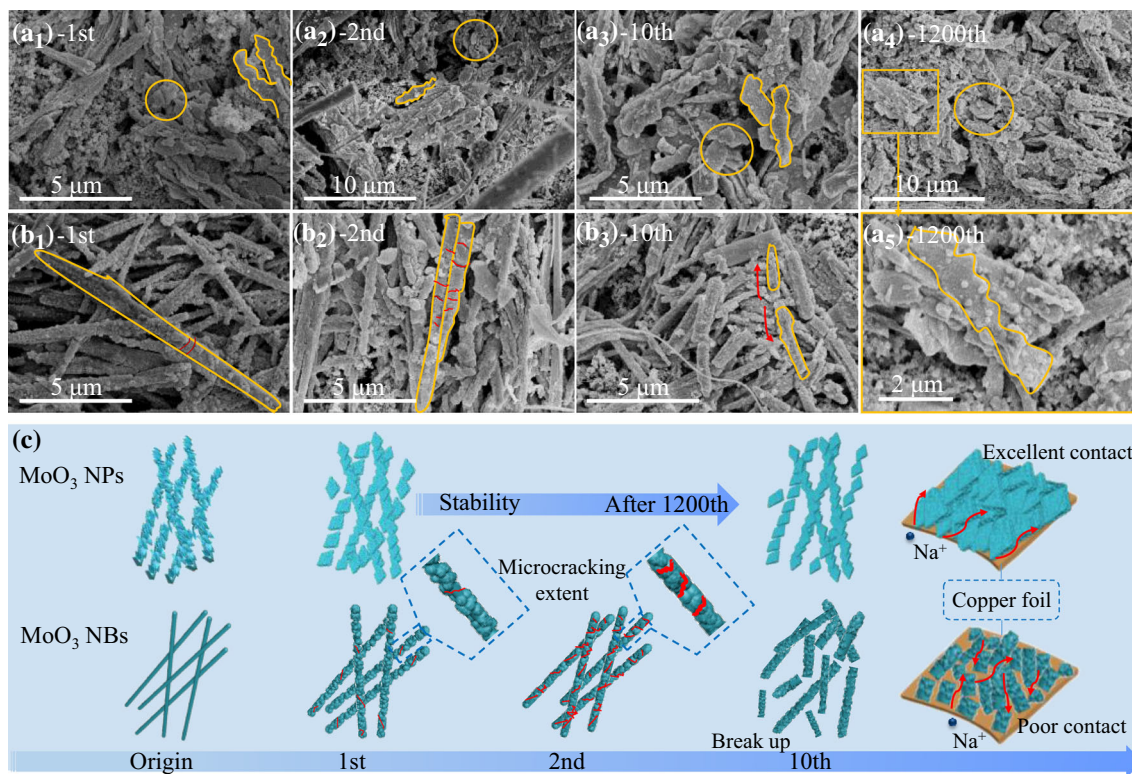


**Figure 6** FESEM images of MoO<sub>3</sub> NPs (**a**<sub>1</sub>, **a**<sub>2</sub>, **a**<sub>3</sub>) and MoO<sub>3</sub> NBs (**b**<sub>1</sub>, **b**<sub>2</sub>, **b**<sub>3</sub>) after 1st, 2nd, 10th, respectively; FESEM images of MoO<sub>3</sub> NPs (**a**<sub>4</sub>, **a**<sub>5</sub>) after 1200th; schematics of micro-topography degradation in two electrodes during discharge–charge process (**c**).

NBs electrode is higher than that MoO<sub>3</sub> NPs electrode, which provide more experimental evidence for low transformation of MoO<sub>3</sub> NBs electrode. In addition, as is shown in Fig. 7d, when desodiation at 3 V, the fraction of Mo<sup>4+</sup> (233.2, 230.1 eV) in MoO<sub>3</sub> NBs are higher than the Mo<sup>4+</sup> in MoO<sub>3</sub> NPs electrode (233.2, 230.1 eV), which indicates that more Na<sup>+</sup> was trapped in the MoO<sub>3</sub> NBs structure than in MoO<sub>3</sub> NPs [43]. This leads to trapped sodium ions that cannot participate in subsequent cycles. However, MoO<sub>3</sub> NPs can ensure that the embedded sodium ions are removed more smoothly than MoO<sub>3</sub> NBs. This may be related to the stable structure and structural integrity of MoO<sub>3</sub> NPs during repeated cycling. Taken together, these results suggest that the excellent electrochemical performance of MoO<sub>3</sub> NPs is attributed to the high reversible reaction during repeated cycling.

## Conclusions

We report a facile and green synthesis method of MoO<sub>3</sub> NPs from Mo-MOFs. The nanoplate structure is the result of growth from lower anisotropy. When used as an anode for SIBs, the MoO<sub>3</sub> NPs show 154 mAh g<sup>-1</sup> superior reversible capacity at a current density of 50 mA g<sup>-1</sup> after 1200 cycles. This is nearly three times than that of MoO<sub>3</sub> NBs (ca. 49 mAh g<sup>-1</sup>). The nanoplate structure of MoO<sub>3</sub> NPs can relieve the stress caused by expansion of volume during discharge–charge process, which prevents pulverization and keeps the micromorphology stability. This study has also shown that the high transformation made contribution to excellent electrochemical performance of MoO<sub>3</sub> NPs. This work offers new insight into the design of structural morphologies to prevent pulverization in other anode materials during repeated cycling.

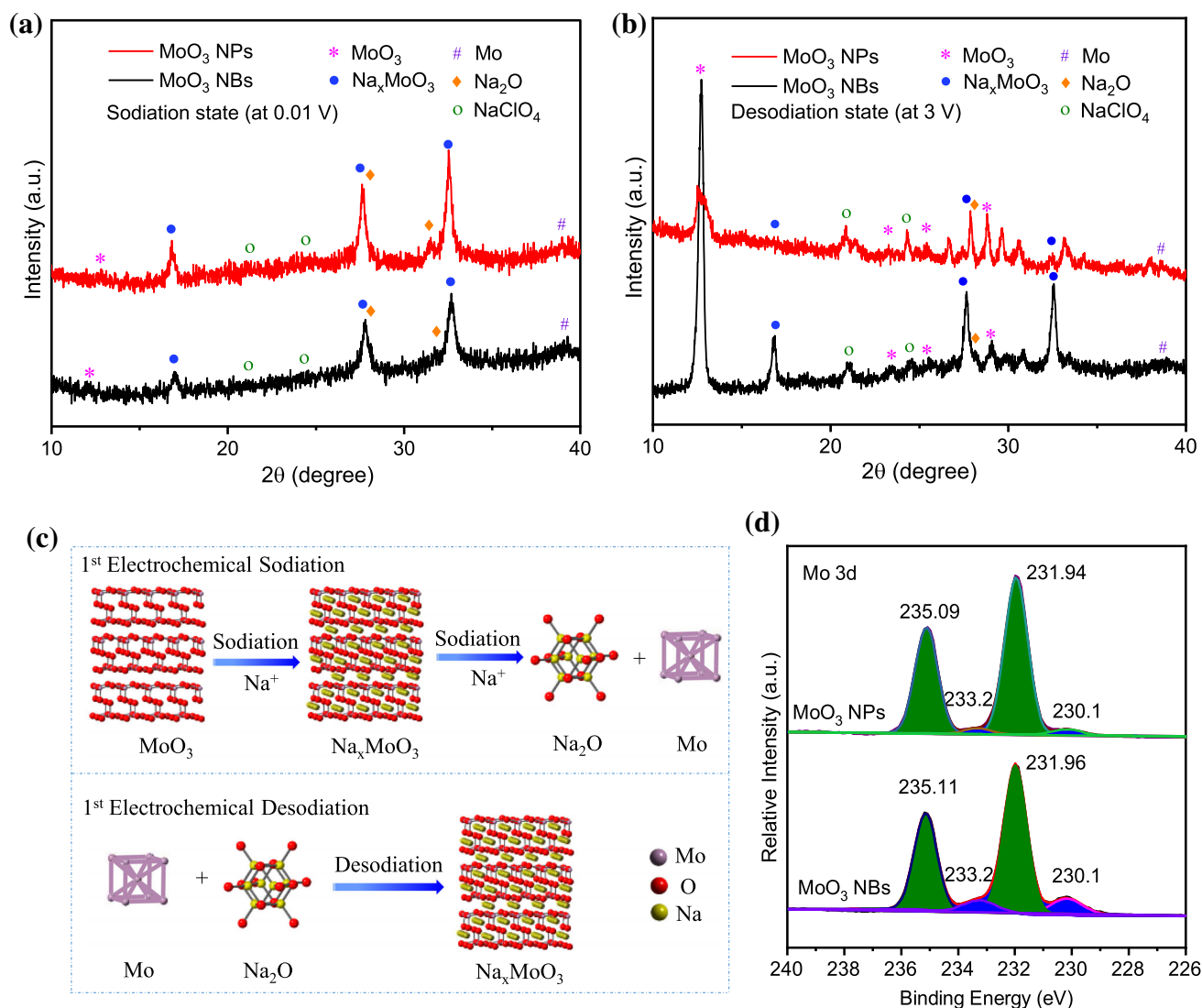


**Figure 7** Ex situ XRD of MoO<sub>3</sub> NBs and MoO<sub>3</sub> NPs at the sodiation (at 0.01 V) (a) and desodiation (at 3 V) (b) state; c crystal structure evolution of electrode for SIBs during the initial

electrochemical discharge–charge process; d Mo 3d of MoO<sub>3</sub> NBs and MoO<sub>3</sub> NPs at the desodiation state (at 3 V).

## Acknowledgements

This study was funded by the National Natural Science Foundation of China (No. 41572034) and the Guangxi Natural Science Foundation (No. 2018GXNSFAA294012).

## Compliance with ethical standards

**Conflict of interest** The authors declare that they have no conflict of interest.

**Electronic supplementary material:** The online version of this article (<https://doi.org/10.1007/s108>

53-020-04788-z) contains supplementary material, which is available to authorized users.

## References

- [1] Tarascon JM (2010) Is lithium the new gold? *Nat Chem* 2:510
- [2] Slater MD, Kim D, Lee E, Johnson CS (2013) Sodium-ion batteries. *Adv Funct Mater* 23:947–958
- [3] Li W, Hu S, Luo X, Li Z, Sun X, Li M, Liu F, Yu Y (2017) Confined amorphous red phosphorus in MOF-derived N-doped microporous carbon as a superior anode for sodium-ion battery. *Adv Mater* 29:1–8

- [4] Liu H, Jia M, Zhu Q, Cao B, Chen R, Wang Y, Wu F, Xu B (2016) 3D-0D graphene-Fe<sub>3</sub>O<sub>4</sub> quantum dot hybrids as high-performance anode materials for sodium-ion batteries. *ACS Appl Mater Interfaces* 8:26878–26885
- [5] Liu Y, Cheng Z, Sun H, Arandiyan H, Li J, Ahmad M (2015) Mesoporous Co<sub>3</sub>O<sub>4</sub> sheets/3D graphene networks nanohybrids for high-performance sodium-ion battery anode. *J Power Sources* 273:878–884
- [6] Wang B, Wang G, Cheng X, Wang H (2016) Synthesis and electrochemical investigation of core-shell ultrathin NiO nanosheets grown on hollow carbon microspheres composite for high performance lithium and sodium ion batteries. *Chem Eng J* 306:1193–1202
- [7] Wang Y, Deng Q, Xue W, Jian Z, Zhao R, Wang J (2018) ZnO/rGO/C composites derived from metal-organic framework as advanced anode materials for Li-ion and Na-ion batteries. *J Mater Sci* 53:6785–6795. <https://doi.org/10.1007/s10853-018-2003-3>
- [8] Sreedhara MB, Santhosha AL, Bhattacharyya AJ, Rao CNR (2016) Composite of few-layer MoO<sub>3</sub> nanosheets with graphene as a high performance anode for sodium-ion batteries. *J Mater Chem A* 4:9466–9471
- [9] Riley LA, Lee SH, Gedvilias L, Dillon AC (2010) Optimization of MoO<sub>3</sub> nanoparticles as negative-electrode material in high-energy lithium ion batteries. *J Power Sources* 195:588–592
- [10] Xia W, Xu F, Zhu C, Xin HL, Xu Q, Sun P, Sun L (2016) Probing microstructure and phase evolution of  $\alpha$ -MoO<sub>3</sub> nanobelts for sodium-ion batteries by in situ transmission electron microscopy. *Nano Energy* 27:447–456
- [11] Spahr ME, Novak P, Haas O, Nesper R (1995) Electrochemical insertion of lithium, sodium, and magnesium in molybdenum(VI) oxide. *J Power Sources* 54:346–351
- [12] McDowell MT, Xia SM, Zhu T (2016) The mechanics of large-volume-change transformations in high-capacity battery materials. *Extreme Mech Lett* 9:480–494
- [13] Wu K, Zhan J, Xu G, Zhang C, Pan D, Wu M (2018) MoO<sub>3</sub> nanosheet arrays as superior anode materials for Li- and Na-ion batteries. *Nanoscale* 10:16040–16049
- [14] Ding J, Abbas SA, Hanmandlu C, Lin L, Lai C, Wang P, Li L, Chu C, Chang C (2017) Facile synthesis of carbon/MoO<sub>3</sub> nanocomposites as stable battery anodes. *J Power Sources* 348:270–280
- [15] Zhang X, Fu C, Li J, Yao C, Lu T, Pan L (2017) MoO<sub>3</sub>/reduced graphene oxide composites as anode material for sodium ion batteries. *Ceram Int* 43:3769–3773
- [16] Yang C, Lu H, Li C, Wang L, Wang H (2018) Spatially-confined electrochemical reactions of MoO<sub>3</sub> nanobelts for reversible high capacity: critical roles of glucose. *Chem Eng J* 337:1–9
- [17] Wang Z, Madhavi S, Lou XW (2012) Ultralong  $\alpha$ -MoO<sub>3</sub> nanobelts: synthesis and effect of binder choice on their lithium storage properties. *J Phys Chem C* 116:12508–12513
- [18] Xia Q, Zhao H, Du Z, Zeng Z, Gao C, Zhang Z, Du X, Kulka A, Świerczek K (2015) Facile synthesis of MoO<sub>3</sub>/carbon nanobelts as high-performance anode material for lithium ion batteries. *Electrochim Acta* 180:947–956
- [19] Lee S-H, Kim Y-H, Deshpande R, Parilla PA, Whitney E, Gillaspie DT, Jones KM, Mahan AH, Zhang S, Dillon AC (2008) Reversible lithium-ion insertion in molybdenum oxide nanoparticles. *Adv Mater* 20:3627–3632
- [20] Jiang Y, Sun M, Ni J, Li L (2019) Ultrastable sodium storage in MoO<sub>3</sub> nanotube arrays enabled by surface phosphorylation. *ACS Appl Mater Interfaces* 11:37761–37767
- [21] Meduri P, Clark E, Kim JH, Dayalan E, Sumanasekera GU, Sunkara M (2012) MoO<sub>3-x</sub> nanowire arrays as stable and high-capacity anodes for lithium ion batteries. *Nano Lett* 12:1784–1788
- [22] Cao D, Dai Y, Xie S, Wang H, Niu C (2018) Pyrolytic synthesis of MoO<sub>3</sub> nanoplates within foam-like carbon nanoflakes for enhanced lithium ion storage. *J Colloid Interface Sci* 514:686–693
- [23] Chen J, Lou X (2012) SnO<sub>2</sub> and TiO<sub>2</sub> nanosheets for lithium-ion batteries. *Mater Today* 15:246–254
- [24] Cao X, Zheng B, Shi W, Yang J, Fan Z, Luo Z, Rui X, Chen B, Yan Q, Zhang H (2015) Reduced graphene oxide-wrapped MoO<sub>3</sub> composites prepared by using metal-organic frameworks as precursor for all-solid-state flexible supercapacitors. *Adv Mater* 27:4695–4701
- [25] Martin-Zarza P, Arrieta J, MuAoz-Roca M, Gili P (1993) Synthesis and characterization of new octamolybdates containing imidazole, 1-methyl- or 2-methyl-imidazole co-ordinatively bound to molybdenum. *J Chem Soc Dalton Trans.* <https://doi.org/10.1039/DT9930001551>
- [26] Lou X, Zeng H (2002) Hydrothermal synthesis of  $\alpha$ -MoO<sub>3</sub> nanorods via acidification of ammonium heptamolybdate tetrahydrate. *Chem Mater* 14:4781–4789
- [27] Li S, Hou H, Huang Z, Liao H, Qiu X, Ji X (2017) Alternating voltage introduced [001]-oriented  $\alpha$ -MoO<sub>3</sub> microrods for high-performance sodium-ion batteries. *Electrochim Acta* 245:949–956
- [28] Cai Y, Yang H, Zhou J, Luo Z, Fang G, Liu S, Pan A, Liang S (2017) Nitrogen doped hollow MoS<sub>2</sub>/C nanospheres as anode for long-life sodium-ion batteries. *Chem Eng J* 327:522–529
- [29] Qiu J, Yang Z, Li Y (2015) N-doped carbon encapsulated ultrathin MoO<sub>3</sub> nanosheets as superior anodes with high capacity and excellent rate capability for Li-ion batteries. *J Mater Chem A* 3:24245–24253

- [30] Ji H, Liu X, Liu Z, Yan B, Chen L, Xie Y, Liu C, Hou W, Yang G (2015) In situ preparation of sandwich  $\text{MoO}_3/\text{C}$  hybrid nanostructures for high-rate and ultralong-life supercapacitors. *Adv Funct Mater* 25:1886–1894
- [31] Ma F, Yuan A, Xu J, Hu P (2015) Porous  $\alpha\text{-MoO}_3/\text{MWCNT}$  nanocomposite synthesized via a surfactant-assisted solvothermal route as a lithium-ion-battery high-capacity anode material with excellent rate capability and cyclability. *ACS Appl Mater Interfaces* 7:15531–15541
- [32] Hariharan S, Saravanan K, Balaya P (2013)  $\alpha\text{-MoO}_3$ : a high performance anode material for sodium-ion batteries. *Electrochem Commun* 31:5–9
- [33] Liu Y, Zhang B, Xiao S, Liu L, Wen Z, Wu Y (2014) A nanocomposite of  $\text{MoO}_3$  coated with PPy as an anode material for aqueous sodium rechargeable batteries with excellent electrochemical performance. *Electrochim Acta* 116:512–517
- [34] Guo J, Sun A, Chen X, Wang C, Manivannan A (2011) Cyclability study of silicon–carbon composite anodes for lithium-ion batteries using electrochemical impedance spectroscopy. *Electrochim Acta* 56:3981–3987
- [35] Xu Y, Zhou M, Wang X, Wang C, Liang L, Grote F, Wu M, Mi Y, Lei Y (2015) Enhancement of sodium ion battery performance enabled by oxygen vacancies. *Angew Chem Int Ed Engl* 54:8768–8771
- [36] Li Y, Wang D, An Q, Ren B, Rong Y, Yao Y (2016) Flexible electrode for long-life rechargeable sodium-ion batteries: effect of oxygen vacancy in  $\text{MoO}_{3-x}$ . *J Mater Chem A* 4:5402–5405
- [37] Liu T-C, Pell WG, Conway BE, Roberson SL (1998) Behavior of molybdenum nitrides as materials for electrochemical capacitors: comparison with ruthenium oxide. *J Electrochem Soc* 145:1882–1888
- [38] Wang J, Polleux J, Lim J, Dunn B (2007) Pseudocapacitive contributions to electrochemical energy storage in  $\text{TiO}_2$  (Anatase) nanoparticles. *J Phys Chem C* 111:14925–14931
- [39] Chao D, Zhu C, Yang P, Xia X, Liu J, Wang J, Fan X, Savilov SV, Lin J, Fan HJ, Shen ZX (2016) Array of nanosheets render ultrafast and high-capacity Na-ion storage by tunable pseudocapacitance. *Nat Commun* 7:12122
- [40] Mukhopadhyay A, Sheldon BW (2014) Deformation and stress in electrode materials for Li-ion batteries. *Prog Mater Sci* 63:58–116
- [41] Zhao Y, Ding C, Hao Y, Zhai X, Wang C, Li Y, Li J, Jin H (2018) Neat design for the structure of electrode to optimize the lithium-ion battery performance. *ACS Appl Mater Interfaces* 10:27106–27115
- [42] Yan P, Zheng J, Gu M, Xiao J, Zhang J, Wang C (2017) Intragranular cracking as a critical barrier for high-voltage usage of layer-structured cathode for lithium-ion batteries. *Nat Commun* 8:14101
- [43] Kim H, Cook J, Lin H, Ko J, Tolbert S, Ozolins V, Dunn B (2017) Oxygen vacancies enhance pseudocapacitive charge storage properties of  $\text{MoO}_{3-x}$ . *Nat Mater* 16:454–460

**Publisher's Note** Springer Nature remains neutral with regard to jurisdictional claims in published maps and institutional affiliations.